Automated Satellite-based Landslide Identification Product for Nepal

1. *Jessica V. Fayne
   Department of Geography
   University of California- Los Angeles,
   Los Angeles, CA, 90024 United States
   Email: jfayne@g.ucla.edu
2. Aakash Ahamed
   Department of Geophysics
   Stanford University
   Stanford, CA, 94305 United States
3. Justin Roberts-Pierel
   Department of Physics and Astronomy
   University of South Carolina
   Columbia, SC, 29208 United States
4. Amanda C. Rumsey
   Department of Geography
   U.S. Census Bureau
   Suitland, MD, 20746 United States
5. Dalia Kirschbaum, PhD
   Hydrologic Sciences Laboratory, Code 617
   NASA Goddard Space Flight Center
   Greenbelt, MD, 20771

*** Corresponding Author**

Abstract

Landslide event inventories are a vital resource for landslide susceptibility and forecasting applications. However, landslide inventories can vary in accuracy, availability, and timeliness as a result of varying detection methods, reporting, and data availability. This study presents an approach to use publicly available satellite data and open source software to automate a landslide detection process called the Sudden Landslide Identification Product (SLIP). SLIP utilizes optical data from the Landsat 8 OLI sensor, elevation data from the Shuttle Radar Topography Mission (SRTM), and precipitation data from the Global Precipitation Measurement (GPM) mission to create a reproducible and spatially customizable landslide identification product. The SLIP software applies change detection algorithms to identify areas of new bare-earth exposures that may be landslide events. The study also presents a precipitation monitoring tool that runs alongside SLIP called the Detecting Real-time Increased Precipitation (DRIP) model that helps identify the timing of potential landslide events detected by SLIP. Using SLIP and DRIP together, landslide detection is improved by reducing problems related to accuracy, availability, and timeliness that are prevalent in the state-of-the-art of landslide detection. A case study and validation exercise was performed in Nepal for images acquired between 2014 and 2015. Preliminary validation results suggest 56% model accuracy, with errors of commission often resulting from newly cleared agricultural areas. These results suggest that SLIP is an important first attempt in an automated framework that can be used for medium resolution regional landslide detection, although it requires refinement before being fully realized as an operational tool.

Keywords: Remote Sensing, Landslides, Automation, Classification, Disasters

1. Introduction

Landslide inventories are critical for creating and evaluating susceptibility maps, determining relationships between landslide occurrences and triggering events, and informing emerging prediction techniques (Kirschbaum et al., 2009). However, the availability, accuracy, extent, and applicability of landslide inventories can vary widely depending on the location, compilation methodology, and distribution. As a result, landslide inventories suffer from underreporting at both regional and global scales (Petley et al., 2007; Castellanos Abella and van Westen, 2007; Kirschbaum, 2015). Significant gaps in available landslide information additionally contribute to the shortcomings of landslide inventories due to the lack of routine global monitoring or cataloging systems, such as is available for hurricanes and earthquakes (Kirschbaum, 2009).

There are several standard approaches for generating landslide inventories. Some catalogs are generated from news reports, other media, and personal communication (Petley et al. 2012; Kirschbaum et al. 2010, 2015). While these inventories provide global coverage of landslide activity with dates of occurrence, the reliance on media reports can result in uneven spatial and temporal accuracy due to reporting biases and underreporting in more remote areas. Another challenge to reporting is that landslides that occur secondary to primary disasters like hurricanes or flooding frequently go unreported since impacts are often reported with the primary disaster (Guzzetti, 2000). Event or regional inventories use field surveys, aerial photography, airborne Light Detection and Ranging (LIDAR), or other high-resolution satellite data to map landslides (Brardinoni et al. 2003, Schulz 2004, Xu et al. 2014). While these methods can accurately delineate

landslide events and extent across a study region, in many of these inventories, there is little information on the timing of these events, which can impede the applicability of this data for use in dynamic modeling studies. Additionally, landslide detection using high resolution imagery and DEMs method can hampered by the availability of or access to data, particularly if imagery needs to be purchased from a commercial vendor. Both of these approaches rely on manual digitization and mapping, which is extremely time consuming and is prone to user error.

Publically available remote sensing data present a practical method to supplement existing landslide inventories with spatial and temporal information across large regions. Visual image interpretation (Speight, 1977; Rib and Liang, 1978); computational analysis of passive optical imagery (Landsat, high-resolution commercial imagery); and computational analysis techniques leveraging synthetic aperture radar (SAR) data (Guzzetti et al. 2012, Behling et al 2016) have all been used successfully for landslide identification.

Visual image interpretation has become more common with the growing availability of high resolution imagery and open source software but is subjective, resource intensive, and time consuming due to manual digitization and interpretation. Furthermore, the timing of landslide events is often imprecise with this method. Multispectral image analysis is a popular technique in landslide detection (Cheng et al., 2004; Nichol and Wong, 2005; Martha et al. 2016) due to (i) additional spectral information content of multispectral imagery, (ii) accessibility and free cost of many multispectral sensors (USGS LDAAP, 2016), and (iii) the opportunity for automation to

reduce human inputs and errors. These techniques can limit reporting biases and reduce the time and resources required for event detection (Guzzetti et al., 2012). Spectral landslide detection using multispectral satellite imagery platforms has been demonstrated by a number of studies (Lee and Lee, 2006; Weirich and Blesius, 2007; Martha et al 2010l Li et al 2014). Semi-automated, high resolution change detection methods for landslide identification have also been explored previously (Hölbling et al., 2015). In contrast with methods requiring the visible range of the electromagnetic spectrum, Interferometric Synthetic Aperture Radar (InSAR) detects surface deformation by using phase differencing and has been an effective technique for landslide identification (Singhroy et al., 1998; Czuchlewski et al., 2003; Farina et al., 2006; Zhao et al 2012, Tantianuparp et al. 2013). Other methods using radar coherence measure the correlation of the heights of locally varying elevations to identify rough texture. Changes in the coherence and polarimetry will readily pinpoint surface changes. (Plank et al 2016; Casagli et al. 2017; Modini 2017) While these are incredibly useful features for landslide identification, radar data can be expensive and is typically not as readily available as shorter wavelength multispectral imagery, rendering this method resource intensive and subject to data availability.

The present study focused on the utilization of multispectral image analysis techniques in order to automate the identification and feature extraction of landslides and changes in bare earth. The motivations for this research are to provide a fast and free method to support analyst work in updating or complementing landslide inventories, and providing a 'first guess' of where landslides may occur without the use of proprietary data or image classification software. Nepal was chosen as a case study due to the prevalence of landslide hazards in the region as well as the availability

of validation datasets. Nepal and the Greater Himalayan region (Figure 1) are highly susceptible to landslides due to mountainous topography, active seismicity, and strong seasonal monsoon rains. The region experiences hundreds to thousands of annual fatalities and millions of dollars in losses annually due to landslide events (Dahal and Hasegawa, 2008, Petley 2007). As a result, this region would significantly benefit from additional, publically available landslide inventories that can be used to improve susceptibility and hazard mapping as well as to support disaster response following a major triggering event.

--FIGURE 1 HERE--

This study presents a two sided approach to landslide detection using imagery to identify extent, and precipitation data to identify the timing of the landslide. Using Landsat 8 imagery (USGS EROS 2016) and infrastructure from the Open Science Data Cloud (Stevens et al., 2012), a system was developed to test the feasibility of automated landslide detection using spectral band analysis and ancillary data. The Sudden Landslide Identification Product (SLIP) takes advantage of spectral properties of vegetation, slope, land cover type and soil moisture in bi-weekly (16-day) time steps to identify new areas of bare earth exposure that may represent landslide events. To identify the likely timing of potential landslide events, the Detecting Real-time Increased Precipitation (DRIP) model leverages NASA's Global Precipitation Measurement (GPM) precipitation data to provide a more precise temporal window of occurrence for each potential event. Section 2 reviews the SLIP and DRIP model methodologies, data sources used, and validation procedures. Section 3

outlines the results and discussion of the model impact and applicability. Section 4 provides a conclusion with ideas of future research.

2. Data and Methodology

The Sudden Landslide Identification Product (SLIP) was developed to test the feasibility of automating landslide detection using open source imagery and without the use of proprietary classification software. As a predominant triggering mechanism for landslides is rainfall (Petley et al. 2005), this study also explored the development of precipitation monitoring tools running alongside SLIP to gain insight on local precipitation thresholds necessary for landslides to occur. The python scripts for SLIP and DRIP are available at https://github.com/NASADEVELOP/DRIP-SLIP.

2.1 Data

SLIP combines multiple visible and infrared channels from publically available satellite platforms to approximate visible landscape changes. Topographic slope and soil moisture are also considered to constrain the locations of potential change. Landsat 8 provides updated reflectance data at 30-meter spatial resolution every 16 days with 5 bandwidths in the visual spectrum and 6 bandwidths in the infrared spectrum. Spectral bands from the red, near-infrared, and short wave infrared were used in this study to identify potential landslide scars automatically.

The slope is calculated from a Digital Elevation Model (DEM) and low slopes are masked out in a method described in 2.2. to limit errors of commission in flat areas where landslides are unlikely such as riverbeds, which may have similar red reflectance and moisture characteristics. The DEM was created by filling in remaining voids from the Void Filled 30m resolution Shuttle Radar Topography Mission (SRTM) DEM (USGS SRTM 2001) with the Advanced Spaceborne Thermal Emission and Reflection Radiometer (ASTER) DEM (NASA, METI, LP DAAC 2015). The transition between the ASTER and the SRTM data regions were smoothed by first aggregating the spatial resolution to 90 meters, and then to downsample the resolution back to 30 meters using bilinear resampling. This produces a smoother transition between DEMs as was done in Gallant (2011) Robinson et al (2014).

A 500-meter land cover map from the International Geosphere-Biosphere Programme (IGBP) derived from the MODIS sensor (LP DAAC MCD12Q1, 2012) was used as a mask to eliminate agriculture and urban areas that often experience similar changes in soil moisture and vegetation to that of a landslide. As a reflection of the 500 meter spatial resolution from IGBP, it is expected that the masked out areas may be overestimated in some regions compared with the 30 meter datasets.

2.2 The Sudden Landslide Identification Product (SLIP) Algorithm

SLIP inspects reflectance values and identifies significant changes using four thresholds: i) reflectance increases in the red wavelength band 4 (655 nm), which may indicate bare earth exposure; ii) changes in the SWIR bands 5 and 7 (860nm and 2,200 nm), which indicates changes

in soil moisture; and iii) steep slopes identified by a digital elevation model (DEM), which limits identifications to steep topography; and finally iv) a land cover mask is applied to limit errors of commission in known agricultural areas. Using the Landsat data, 'percent red change' is calculated from a difference between dates in the bands at 655nm. The most recent date is the 'current' image which has clouds flagged as no data. The 'composite' image is a cloud-free composite of previous dates of imagery to ensure as much of the scene can be analyzed and not ignored due to current or historical cloud cover.

Changes in the red band are calculated using the equation:

(1)

$$\%\ Red\ Change\ = (\frac{R655nm_{Current}\ - R655nm_{Composite}}{R655nm_{Composite}})\ *\ 100$$

Equation 1 is applied to each pixel in the latest Landsat scene. Areas that show at least 40% increase in red reflectance were flagged and marked “1” while all other pixels are marked “0”.

SLIP was calibrated from spectral analysis of several landslide events in Nepal by visually identifying landslides and inspecting pixel values for those slides. Analysis of the multispectral Landsat data suggested that increases in red wavelengths (Band 4: 640 – 670 nm) best captured

169 the spectral characteristics of landslides and bare earth exposure in mountainous and forested
170 terrains. However, many landslides are much smaller than this in areal extent, no more than 10
171 Landsat pixels, depending on the shape of the landslide. Therefore, the SLIP model is limited in
172 its ability to detect small landslides.

173

174 Vegetation and soil moisture have been estimated using a variety of spectral indices such as

175 Normalized Difference Water Index (NDWI) (Gao 1996), and the Normalized Multi-band Drought
176 Index (NMDI) (Wang & Qu 2007). These indices are effective for measuring drought and flood
177 conditions and their corresponding effects on vegetation. NMDI is sensitive to soil moisture as
178 well as vegetation, making it an ideal means to measure soil moisture changes over time in areas
179 of sparse vegetation or bare earth, in addition to vegetated areas. As NMDI was created for
180 Moderate Resolution Imaging Spectroradiometer (MODIS) specifications, a *modified* NMDI
181 variable (mNMDI) was created for this study, focusing on similar sensitivities of infrared and
182 short-wave infrared bands on the Landsat sensor.

183

184 The Normalized Multi-band Drought Index (for MODIS) is expressed by:

185 (2)

186 $$NMDI = \frac{R860nm - (R1640nm - R2130nm)}{R860nm + (R1640nm - R2130nm)}$$

187

The modified version omits the MODIS 1640 nm short-wave, as the closest band on Landsat 8 is 1610 nm (band 6) demonstrated poor performance for this task. The modified version is as follows using Landsat 8, bands 5 and 7 as 860 nm and 2200 nm respectively:

(3)

$$mNMDI = \frac{R860nm - R2200nm}{R860nm + R2200nm}$$

Values between -0.2 and 0.2 show higher moisture content, which is clear to see particularly along water bodies. Using the Spectral Characteristics Viewer from USGS (https://landsat.usgs.gov/spectral-characteristics-viewer), the formula can be applied and compared between lawn grass, dry grass, clear water, and rocks/soils. The mNMDI values for lawn grass is 0.5, dry grass is 0.3, clear water is 0, and rocks and dry soils is -0.3. Mixtures of soils, vegetation and water center on 0 with more negative values likely being due to a higher soil mixture, and more positive value being due to a higher vegetation mixture. Variations of these mixtures are likely where fresh soils have been revealed turning over the previous vegetation during landslide events. The change detection algorithm delineates regions of high moisture and assigns the region a value of 1, values outside the region are 0. Table 1 shows how the biweekly, newest composite, called 'today', compares with the previous data called 'historic', with three possible outcomes.

--TABLE 1 HERE--

208 Landslide studies using DEMs often use slope thresholds to eliminate errors of commission
209 (Jimenez-Peralvarez et al 2011). The thresholds and intervals can vary by region, study focus, and
210 DEM resolution. In this model, slope intervals were used to categorize slopes as gentle (0-20°),
211 fairly steep (20-35°), steep (35-45) very steep (45-60°), and extremely steep (60-90°). The
212 distribution is summarized in Figure 2 for Nepal based on the total area in each category from the
213 DEM 30m pixels. A slope value of 20 degrees was used as a minimum threshold for potential
214 landslide initiation points as gentle slopes are less likely to have sudden landslide events. Slope
215 classification values were assigned to each bin to include relative slope information in the final
216 landslide detection, shown in figure 2.

217

218 --FIGURE 2 HERE--

219

220 Values for each flagged pixel (0 - 1) are summed across the 3 layers (red reflectance, soil moisture,
221 and slope threshold) to create a raster image with values 0 - 3. The reflectance and soil moisture
222 criteria are assigned a value of 0 or 1, while values for slope are binned into one of five slope
223 classifications (0.2, 0.4, 0.6, 0.8, and 1) as summarized in Figure 2. Values less than 1 denote that
224 no criteria were met, while values 1 - 2 indicate that at least one criteria was met, and values 2 – 3
225 indicate that both red reflectance and soil moisture criteria were met. Slopes over 20 degrees are
226 assigned a classification of "0.4", and slope pixel values greater than or equal to 0.4 are marked as
227 potential landslide initiation areas when combined with reflectance and moisture flags. Total
228 values of 2.4 and above are interpreted as 'red looking' areas of increased moisture on a high

229 gradient. An example of this is shown in detail in Figure 3 as the landslide scar shows changes in
230 moisture from the recent rainfall event but no reflectance changes, the newly revealed soil from
231 the landslide shows changes in both reflectance and moisture. The third part of the image
232 demonstrates the red reflectance and moisture changes between the first two Landsat scenes.

233 --FIGURE 3 HERE--

234

235 After the thresholding was complete, the International Geosphere-Biosphere Programme (IGBP)
236 MODIS 500 meter land cover map (LP DAAC MCD12Q1, 2012) was used as a mask to eliminate
237 agriculture and urban areas that often experience similar changes in soil moisture and vegetation.
238 All pixels that fall within agriculture or urban areas are excluded from the final SLIP output due
239 to frequent erroneous detections by the algorithm.

240

241 Updated maps of landslide detections are automatically generated for each tile every 16 days and
242 are saved in a GeoTIFF format. As the file names contain the date and Landsat tile location by
243 path/row, users are able to examine any detection that has been made over a particular area by
244 examining the product file names.

245 **2.3 The Detecting Real Time Increased Precipitation (DRIP) Algorithm**

246 While SLIP identifies potential landslides at 30-meter resolution, the identification is limited by
247 the temporal resolution of the Landsat sensor and the pervasiveness of cloud cover in the study

region. Detections can be as frequent as the day the Landsat image was acquired, if the area is cloud-free, but can be limited by up to 3 months during periods of extensive cloud cover, requiring many composited images. If we assume that the SLIP landslide detections are triggered by rainfall and that the peak precipitation during the 16-day temporal window between overpasses coincides with landslide occurrence, landslide detections can be identified in finer temporal windows by monitoring continuous precipitation accumulations in the 16-day period between detections from SLIP.

The Detecting Real-time Increased Precipitation (DRIP) tool was developed (Figure 4) to provide suggested dates to correspond to the SLIP landslide detections. Another advantage of DRIP is that it helps to identify extreme rainfall in near-real time and suggest where potential images may be located as seen in figure 4.

There have been several research efforts to quantify rainfall thresholds for landslide triggering in the study region (Dahal and Hasegawa, 2008, Froehlich et al 1993). In particular, Froehlich (1990) established that in the Himalayan region, small slides and flows can be triggered by between 130-150mm of accumulated rainfall in a 24-hour period, and 180-200mm accumulation in 72 hours. For larger slide events, landslides may be triggered only after exceeding 250 and 350mm of rainfall in a 24 and 72-hour period, respectively. In subsequent research, Dahal (2008) identified that 144mm rainfall accumulation in a 24-hour period substantially increased the risk of landslides. While both of these studies were undertaken using gauge, not satellite data, they do provide a baseline for considering potential triggering thresholds in this region. A study of satellite precipitation products from GPM's predecessor, the Tropical Precipitation Measurement Mission

(TRMM) reveal that orographic precipitation may be underestimated by 5-14 mm (Hashemi et al 2017). As GPM uses some of the same satellites as TRMM in the multi-satellite merged product, it is expected that GPM and TRMM will have similar biases. To use the GPM data in this analysis, we present lower thresholds than were established in the gauge studies.

--FIGURE 4 HERE--

To associate the intense rainfall events to probable landslides, satellite precipitation data is gathered in near real-time from the Global Precipitation Measurement mission Integrated Multisatellite Retrievals for GPM (IMERG) Early product (Huffman et al 2015), which is available in half-hourly time steps and 0.1 degree spatial resolution with a latency of 4 hours. DRIP collects the half-hourly IMERG data in a moving 16-day window to accommodate the SLIP output, and constructs rainfall accumulations in 24, 48, and 72-hour moving windows within the 16-day span, using threshold values of 145mm, 170mm, and 195mm respectively.

To suggest the landslide event date within the 16-day window, DRIP selects the 24, 48, and 72-hour data that exceed the established rainfall thresholds. When there are multiple dates that exceed the rainfall threshold, the largest rainfall event is chosen. While it is uncertain which of the major storms contributed to the landslide, it is likely that the landslide may be associated with the passage of the storm, either during or after the event. Similarly, where the 24-hour thresholds are met, the

288 additional 48 and 72-hour thresholds are not considered, even if the threshold is reached for the
289 longer duration.

290 The pixels with the precipitation values exceeding the thresholds from the 24, 48, and 72-hour
291 windows are combined into one product, with a separate raster data layer containing metadata of
292 the original dates that contributed to the combined product. To use the DRIP outputs with SLIP,
293 the combined thresholds are given a flag of "2" in a similar manner to the three SLIP flags. The
294 coordinates of each pixel extent are used to assign the additional DRIP flag to the SLIP output, as
295 the spatial resolution of the GPM precipitation is much coarser than the Landsat SLIP product.

296 When the "2" flag is added to the SLIP product, SLIP-DRIP total values above 4 have

297 corresponding precipitation values exceeding the DRIP threshold, and will have specified dates
298 and times for the extreme rainfall that may suggest a trigger for the potential landslide(s). This
299 process can offer insight into the potential timing of the landslides detected as well as on regional
300 precipitation thresholds that may result in slope failures.

301 **2.4 Automation and Preprocessing**

302

303 SLIP and DRIP require the open source libraries NumPy (http://numpy.org) for processing raster
304 arrays and GDAL (http://gdal.org) for reading, writing, and archiving geospatial data. The SLIP
305 program preprocesses Landsat 8 data before performing change detection analyses and uses an
306 external program to download Landsat 8 data (Hagolle et al., 2016). The workflow for all the SLIP
307 and DRIP components can be found in Figure 5. The SLIP and DRIP documentation

(https://github.com/NASA-DEVELOP/DRIP-SLIP) details the list of package dependencies, as well as installation instructions. The SLIP and DRIP algorithms were tested using a server hosted by the Open Science Data Consortium (Stevens et al., 2012).

FIGURE 5:

2.4.1 SLIP Automation

The SLIP program can download new Landsat 8 scenes from USGS Earth Explorer (www.usgs.earthexplorer.com, USGS LP DAAC 2016) each day as scenes are made available. When a new Landsat scene is available in the study area, the program proceeds to the preprocessing and change detection stages. The Landsat 8 satellite captures images of the Nepal and Himalayan region every 16 days at 30-meter resolution. For this application, SLIP downloads Landsat scenes (Paths 139-144; Rows 39-41) as they become available.

When each new scene is downloaded, the red band (band 4: 655 nm), short-wave infrared (SWIR band 7: 2,200 nm), near infrared (NIR band 5: 860 nm), panchromatic band 8, and quality assurance (QA) bands are extracted and stored in a temporary directory. Each Landsat tile in the study region has a local repository of the previous 10 scenes at that tile. To address issues of persistent cloud cover, compositing tasks mask out cloud pixels, replacing missing data with data from the previous 10 scenes to maximize cloud free observations. Cloud identification procedures mask pixels based on the Landsat 8 QA band and a 96% reflectance threshold in the panchromatic

band. All pixels flagged as clouds are replaced with corresponding cloud free pixels from the previous scenes, beginning with the most recent. This process iterates until either all pixels in the current scene are cloud-free, or all 10 scenes have been used in the backfill. The newest image is then compared to the composited image.

2.4.2 DRIP Automation

The DRIP program downloads the GPM IMERG data in near real-time through the NASA Precipitation Processing System (PPS) FTP server (ftp://jsimpson.pps.eosdis.nasa.gov/). The processing latency for the half-hourly GPM IMERG dataset is approximately 4-6 hours from observation. This data is an 'early run' initial processing of the data without gauge calibration (Huffman et al 2015) and is not considered 'research grade', which are produced more than a month after the satellite observation. For the near real-time application of landslide identification and dating, it is deemed more important to have a more rapid intake of available precipitation data as it is available.

The FTP server provides the GPM data on a global grid in HDF file format. As data is made available, it is downloaded, subset to the region as a GeoTIFF file, and accumulations are created for the 24, 48, and 72-hour moving windows. Because intense short duration precipitation is more likely to cause landslides in this region compared to lower intensity longer duration accumulations (Froehlich et al 1990, 1993; Dahal et al 2008; Petley 2010), the 24-hour accumulation carries more significance than the 48 and 72-hour accumulations. The python script uses this priority to create a set of three raster images for the 16-day period matching the Landsat SLIP output. The first image represents points where the rainfall thresholds have been triggered with the triggering

values, the second ‘image’ contains the date as a pixel value, and the third raster is the triggering flag that works directly with the SLIP outputs.

3. Validation

The SLIP model outputs were validated to assess SLIP’s landslide identification capabilities on a regional scale within Nepal. Two SLIP detection raster maps were selected for five Landsat tiles covering Nepal (Figure 6). For each tile, one raster falling during the monsoon season (June through September) and another raster falling outside of the monsoon season (October through May) were selected for validation. In total, 10 dates were selected for validation.

--FIGURE 6 HERE—

To prepare the SLIP data for validation, SLIP detection images were masked to only retain pixels with values greater than 2.4, representing areas that exceeded the three previously mentioned thresholds and areas that met the land cover condition. Using GIS software, each raster was converted to a polygon. A 60-meter buffer was then applied to each polygon to cluster discrete polygons into larger landslide events. This technique ensures that neighboring detected pixels with a small gap in detection will be considered to be the same landslide event. As there may be hundreds of landslide detections that fit the criteria than can be efficiently validated manually, a

sample of 10% of the landslide detections were extracted from each of the 10 buffered shapefiles for validation.

The landslide event polygons were validated using a Google Earth scene following the date of the detection. Google Earth Pro (desktop) was used to reference the landslides by inputting the coordinates of the potential landslides into the search and modifying the time slider to match a time near the estimated landslide event. Two analysts visually assessed each of the landslide event polygons independently and assigned them to an appropriate classification category. The 9 classification categories assigned for an event included: Landslide occurring in a Forest or as a result of Glacier Melt, and No Landside as Terrace, Barren, Agriculture, Mountainside/No Vegetation Change, Riverbed, and Urban, as well as Unidentifiable if the surface could not be clearly seen from the Google Earth reference imagery. If a SLIP event was classified as a Landslide, the event was assigned a value of one representing a positive landslide detection, No

Landslide was assigned a value of zero representing a false positive landslide detection, and Unidentifiable was also assigned a value of zero due to the inability to positively identify a landslide. The non-landslide classifications help to quantify deficiencies in the algorithm, particularly, where there are high errors of commission for a certain type of 'non-landslide'.

A confidence rating was assigned to each SLIP event detection based on the combined assessment of the analysts. A rating of 'high confidence' was given to detections where both reviewers agreed that a positive detection occurred, a rating of 'low confidence' was given to detections where only

one of the two reviewers believed that a positive detection occurred, and a rating of 'no confidence' was given to the detections where both reviewers agreed that the detection was a false detection.

4. Results and Discussion

The SLIP model outputs were validated using 15-meter resolution or higher in Google Earth imagery to assess landslide identification capabilities on a regional scale within Nepal (Figure 7).

The SLIP classification results are displayed in Table 2. In the 10 validation scenes, SLIP detected "High Confidence" landslides with accuracies ranging from 12% to 56%. The average "High Confidence" accuracy over Nepal is 27%. When "Low Confidence" landslides are included in the assessment, detection accuracies increase significantly, ranging from 32% to 83%. This averages out to an overall accuracy of 56% for "combined detection" over the entire region.

--FIGURE 7 HERE--

Multiple regional characteristics could influence inconsistencies in results among tiles. The SLIP algorithm is designed to detect areas that experience changes in vegetation and soil moisture which

exceed a certain slope threshold. Because Nepal is predominantly mountainous, agricultural and terraced areas commonly experience soil moisture changes due to irrigation and vegetation changes due to harvesting. These areas are often found on slopes exceeding the current SLIP threshold. The land cover classification criterion was added to the product to eliminate false positive detections in urban and agricultural areas, but due to the coarse resolution of publicly available land cover maps, agriculture-related false detections persist. The tiles that fall within the agricultural region of Nepal (path/row 144/40 and 141/41 are highlighted in Table 2) have much lower combined landslide confidence accuracies than other tiles covering mountainous regions and uninhabited regions of Nepal. The agricultural tiles have combined landslide confidence accuracies ranging from 29-58% while mountainous tiles have accuracies ranging from 54-83%.

--TABLE 2 HERE—

Errors of commission can also result from unmasked clouds that may match the soil and brightness criteria of SLIP. Though cloud masking and buffering techniques are included in the model, some clouds can be difficult to distinguish from the land surface, particularly in areas of snow-capped mountains. Future advances in cloud masking algorithms and the incorporation of thermal imagery could serve to enhance the cloud mask and further reduce errors of commission.

SLIP was also analyzed to detect performance variations due to seasonality. Over the five tiles analyzed during validation, four of the five tiles showed 4 to 14% increase in high confidence landslide detection performance during the monsoon season (Table 2). When used without DRIP, SLIP is likely to perform better during the monsoon season due to rainfall-induced landslide occurrence, as extreme rainfall events are the primary driver of landslide occurrences in the country. Combining DRIP with SLIP has the potential to decrease the number of false detections during the monsoon and dry seasons.

Because the dates are not precisely defined in the imagery alone, existing landslide databases such as the Global Landslide Catalog (GLC) (Kirschbaum et al 2010), International Disaster Database (Sapir and Mission 1992), and the Durham Fatal Landslide Database (Petley 2012) can be used to validate DRIP. To this end, the DRIP validation requires dates to be associated with each landslide event, with a preference given to event entries with precise times. However, because of reporting biases affecting the dates and times in existing inventories, a more constricted catalog with a minimal date based biases will be compiled for Nepal from the previously mentioned sources as well as additional sources. The new compilation database is currently in progress and is not available for validation of the current work, but it will be discussed in the validation of future improvements to the SLIP and DRIP algorithms. Using a more comprehensive database will allow more rigorous analysis using inventories. Once complete, the DRIP time series for each pixel surrounding the respective landslide event will be used to estimate the date and time of the landslide. The estimated time from DRIP can then be compared with the actual time from the reported landslide.

449

450 The DRIP precipitation time series for the Jure Sunkoshi Landslide featured in Figure 3 is shown
451 in Figure 8 and highlights the intense precipitation in the hours leading up to the event. The rainfall
452 events leading up to the slide were spread out as major storms every few days, culminating in one
453 rainfall event with 38mm of rain falling in one hour. This is significantly higher precipitation
454 compared to the average 2mm per hour for the pixel.

455

456 --FIGURE 8 HERE--

457

458 Limitations of the proposed methodology stem from calibration and sensitivity of the spectral
459 bands used within the SLIP algorithm as well as limitations of the validation datasets. Data from
460 previous Landsat satellites were evaluated to determine if these data can be used to construct a
461 longer record. However, analysis of Landsat 7 and 5 indicated that the bands used in these satellites
462 diverged too much from those available from Landsat 8. The sensitivity of the algorithm has been
463 developed to function with characteristics that are common globally but has so far only been tested
464 in the Nepal region. Calibration for SLIP was performed for a small group of landslides in Nepal,
465 and therefore is limited by the quality and availability of the catalog for this region. Validation of
466 this model is also subject to uncertainties due to the analysts' interpretation of landslides within
467 the area and the availability of imagery within Google Earth. If the algorithm detected a landslide
468 but there is not sufficient multi-temporal views or look angles from high resolution imagery to
469 confirm the landslide event, the validation may be biased. Potential differences between analysts'

visual classification were addressed by requiring two classifications for each SLIP detection; however, the limited availability of high resolution imagery. If this model is considered to be used in other regions, the SLIP model would need to be calibrated and tested with high quality landslide inventory information due to the presence of different land cover types, terrain, and atmospheric effects such as trace cloud cover and haze which could not be removed by the Landsat cloud mask and atmospheric correction.

Lastly, there are issues regarding the high level of false alarms in the current algorithm. As discussed above, the false alarms can result from physical phenomena such as seasonal vegetation changes, riverbeds, agricultural lands, and urban areas. Additional false alarms may result from sensor and algorithm sensitivities such as seasonal brightness changes, cloud and edge artifacts from the multi-day composite process, and sensor abnormalities (such as scan errors). As a result, this algorithm still requires manual validation of potential landslide detections before they should be considered as true landslide point.

5. Conclusions

Two automated tools, SLIP and DRIP, have been developed to identify potential location and timing of newly triggered landslides seen from Landsat 8 imagery using spectral thresholding algorithms and precipitation data from GPM. These tools have the ability to map new landslide events and estimate specific dates for the landslide occurrence.

The SLIP algorithm demonstrates how publically-available Landsat 8 data can be utilized for automated and rapid detection of potential landslide events. However, the limitations of the current system may impact its applicability or transferability across users or regions. The system detects changes on the surface within areas of high slopes where there is an indication that the ground is wet. Therefore, the algorithm requires adjustment to the local elevation and slope characteristics in order to identify the crowns or initiation points that are on regionally different gradients. In addition, this algorithm may not be sensitive to seismically triggered landslides where moisture is not a significant cause for the event. Slow moving creep events that occur on more gradual slopes and shallow debris flows with narrow widths but long runouts are also less likely to be detected due to the masking out of more gradually sloping areas, the 30 m spatial resolution of the Landsat data, and the expectation of a drastic reflectance difference between scenes. The Landsat pixel resolution also limits the detection of smaller landslides (less than 30-45 meters in width).

SLIP enables automatic landslide identification with the intention to reduce the amount of time required to interpret satellite imagery manually. This method covers larger areas and can digest more imagery compared to supervised classification, which can be useful in the context of research and situational awareness of potentially impacted areas following a major event. The SLIP algorithm requires additional refinement to remove errors from the temporal compositing before it can be fully realized as an operational tool, but is an important first attempt in an automated operational framework for medium-resolution regional landslide detection. The DRIP algorithm can be similarly used as a standalone product to aid in the manual identification of major

precipitation events in near real-time that may cause landslides and flooding events. More testing of regional suitability and applicability is required before these tools can be implemented for disaster relief applications.

Acknowledgements

This research was funded by a grant from the NASA Applied Sciences Program as a part of the NASA DEVELOP National Program. We would like to thank NASA DEVELOP and all of the Himalayan Disasters Team members and advisors at NASA Goddard Space Flight Center for supporting and guiding the research. We also want to thank Dr. John Bolten, who is the lead science advisor for NASA DEVELOP at Goddard Space Flight Center, and Mr. Thomas Stanley whose expertise in landslide mapping contributed useful feedback on our methods. The International Centre on Integrated Mountain Development (ICIMOD) also supported the NASA DEVELOP effort through collaboration, data sharing, and student participation. This work made extensive use of the server provided by Open Science Data Cloud (OSDC) which was used in all stages of the initial development, testing, and validation of the SLIP and DRIP methods.

References

Brardinoni, F., O. Slaymaker, and M. A. Hassan, 2003: Landslide inventory in a rugged forested watershed: a comparison between air-photo and field survey data. *Geomorphology*, 54, 179–196, doi:10.1016/S0169-555X(02)00355-0.

Behling, R., S. Roessner, D. Golovko, and B. Kleinschmit, 2016: Remote Sensing of Environment Derivation of long-term spatiotemporal landslide activity — A multi-sensor time series approach. Remote Sens. Environ., 186, 88–104, http://dx.doi.org/10.1016/j.rse.2016.07.017.

Castellanos Abella EA, van Westen CJ (2007) Generation of a landslide risk index map for Cuba using spatial multi-criteria evaluation. Landslides 4:311–325. doi:10.1007/s10346-007-0087

Cheng, K.S., Wei, C., Chang, S.C., 2004. Locating landslides using multi-temporal satellite images. Advances in Space Research 33 (3), 96–301.

Czuchlewski, K.R., Weissel, J.K., Kim, Y., 2003. Polarimetric synthetic aperture radar study of the Tsaoling landslide generated by the 1999 Chi-Chi earthquake, Taiwan. Journal of Geophysical Research 108 (F1), 7.1–7.11.

Dahal R.K., Hasegawa S., 2008. Representative rainfall thresholds for landslides in the Nepal Himalaya. Geomorphology 100:429-443.

Farina, P., Colombo, D., Fumagalli, A., Marks, F., Moretti, S., 2006. Permanent scatters for landslide investigations: outcomes from the ESA-SLAM project. Engineering Geology 88, 200– 217.

Froehlich W., Starkel L., 1993 The effects of deforestation on slope and channel evolution in the tectonically active Darjeeling Himalaya. Earth Surface Processes and Landforms, 18: 285–290

Froehlich W., Gil E., Kasza I., Starkel L., 1990 Thresholds in the transformation of slopes and river channels in the Darjeeling Himalaya, India Mountain Research and Development, 10: 301– 312

Gallant, J.C., 2011. Adaptive smoothing for noisy DEMs. Geomorphometry Conference, Redlands, CA, 7–9 September. (Published at: <**http://geomorphometry.org/Gallant2011**>).

Gao, Bo-cai. 1996. NDWI- A normalized difference water index for remote sensing of vegetation liquid water from space. Remote Sensing of Environment 257-266.

Guzzetti F, Cardinali M, Reichenbach P (1994) The AVI project: a bibliographical and archive landslides and floods in Italy. Environ Manag 18:623–633. doi:10.1007/BF02400865

Guzzetti F (2000) Landslide fatalities and the evaluation of landslide risk in Italy. Eng Geol 58:89–107. doi:10.1016/S0013-7952(00)00047-8

Guzzetti F, Mondini AC, Cardinali M, Fiorucci F, Santangelo M, Chang KT (2012) Landslide inventory maps: new tools for an old problem. Earth Sci Rev 112(1–2):42–66

Hagolle O., Nunes V., Lampada T., Mitchell M., Tzotsos A., 2016 Download_landsat_scene.py, GitHub repository, https://github.com/olivierhagolle/LANDSAT-Download

Hölbling, D., Friedl, B. and Eisank, C., 2015. An object-based approach for semi-automated landslide change detection and attribution of changes to landslide classes in northern Taiwan. Earth Science Informatics, 8(2), pp.327-335.

Huffman, G. J., D. T. Bolvin, D. Braithwaite, K. Hsu, R. J. Joyce, and P. Xie, 2015: *Algorithm Theoretical Basis Document (ATBD) for NASA Global Precipitation Measurement (GPM) Integrated Multi-satellitE Retrievals for GPM (IMERG)*. 30 pp. http://pmm.nasa.gov/sites/default/files/document_files/IMERG_ATBD_V4.5.pdf.

Jarvis, A., H.I. Reuter, A. Nelson, E. Guevara, 2008, Hole-filled SRTM for the globe Version 4, available from the CGIAR-CSI SRTM 90m Database (http://srtm.csi.cgiar.org).

Kirschbaum, D.B, T. Stanley, and Y. Zhou (2015), Spatial and temporal analysis of a global landslide catalog, Geomorphology, 249, 4–15, doi:10.1016/j.geomorph.2015.03.016.

Kirschbaum, D.B., Adler, R., Hong, Y., Hill, S. and Lerner-Lam, A., 2010. A global landslide catalog for hazard applications: method, results, and limitations. Natural Hazards, 52(3), pp.561-575.

Kirschbaum, D.B., Adler, R., Hong, Y. and Lerner-Lam, A., 2009. Evaluation of a preliminary satellite-based landslide hazard algorithm using global landslide inventories. Natural Hazards and Earth System Science, 9(3), pp.673-686.

Lee, S., Lee, M.-J., 2006. Detecting landslide location using KOMPSAT 1 and its application to landslide-susceptibility mapping at the Gangneung area, Korea. Advances in Space Research 38 (10), 2261–2271.

Li, Y., Chen, G., Wang, B., Zheng, L., Zhang, Y., & Tang, C. (2013). A new approach of combining aerial photography with satellite imagery for landslide detection. *Natural hazards*, *66*(2), 649-669.

Martha, T. R., Kerle, N., Jetten, V., van Westen, C. J., & Kumar, K. V. (2010). Characterising spectral, spatial and morphometric properties of landslides for semi-automatic detection using object-oriented methods. *Geomorphology*, *116*(1), 24-36.

Martha, T. R., Kamala, P., Jose, J., Kumar, K. V., & Sankar, G. J., 2016. Identification of new Landslides from High Resolution Satellite Data Covering a Large Area Using Object-Based Change Detection Methods. Journal of the Indian Society of Remote Sensing, 1-10.

NASA JPL. 2013. NASA Shuttle Radar Topography Mission Global 1 arc second. NASA LP DAAC. https://doi.org/10.5067/MEaSUREs/SRTM/SRTMGL1.003

NASA LP DAAC, 2016, Landsat 8 Level 1 Reflectance Terrain Corrected. NASA EOSDIS Land Processes DAAC, USGS Earth Resources Observation and Science (EROS) Center, Sioux Falls, South Dakota (https://lpdaac.usgs.gov), accessed January 1, 2016, at https://lta.cr.usgs.gov/L8.

NASA LP DAAC, 2001. ASTER DEM Product. NASA LP DAAC. https://doi.org/10.5067/ASTER/AST14DEM.003

Nichol, J. and Wong, M.S., 2005. Satellite remote sensing for detailed landslide inventories using change detection and image fusion. International Journal of Remote Sensing, 26(9), pp.1913-1926.

Nichol, J., Wong, M.S., 2005. Detection and interpretation of landslides using satellite images. Land Degradation & Development 16, 243–255.

Petley, D. N., S. A. Dunning, and N. J. Rosser, 2005: The analysis of global landslide risk through the creation of a database of worldwide landslide fatalities. *Landslide Risk Management*, O. Hungr, R. Fell, R. Counture, and E. Ebergardt, Eds., Balkema, Amsterdam, 367–374.

Petley, D.N., Hearn, G.J., Hart, A., Rosser, N.J., Dunning, S.A., Oven, K. and Mitchell, W.A., 2007. Trends in landslide occurrence in Nepal. Natural Hazards, 43(1), pp.23-44.

Petley, D., 2012: Global patterns of loss of life from landslides. *Geology*, G33217, 1–4, doi:10.1130/G33217.1. http://geology.gsapubs.org/cgi/doi/10.1130/G33217.1 (Accessed August 6, 2012).

Rib, H.T., Liang, T., 1978. Recognition and identification. In: Schuster, R.L., Krizek, R.J. (Eds.),
Landslide Analysis and Control. : Transportation Research Board Special Report, 176. National Academy of Sciences, Washington, pp. 34–80.
Robinson N., Regetz J., Guralnick R.P., 2014. EarthEnv-DEM90: A nearly-global void-free, multi-scale smoothed, 90m digital elevation model from fused ASTER and SRTM data.
Sapir, D.G., and Misson, C., 1992, The development of a database on disasters: Disasters, v. 16, p. 74–80, doi:10.1111/j.1467-7717.1992.tb00378.x.
Schulz, W. H., 2004: Landslides mapped using LIDAR imagery, Seattle, Washington. *U.S. Geol. Surv.*, Open-File , 1–11.
Singhroy, V., Mattar, K.E., Gray, A.L., 1998. Landslide characterisation in Canada using interferometric SAR and combined SAR and TM images. Advances in Space Research 21, 465–476.
Speight, J.G., 1977. Landform pattern description from aerial photographs. Photogrammetry 32, 161–182.
Tantianuparp, P., X. Shi, L. Zhang, T. Balz, and M. Liao, 2013: Characterization of Landslide Deformations in Three Gorges Area Using Multiple InSAR Data Stacks. Remote Sens., 5, doi:10.3390/rs5062704.
The MODIS MCD12Q1 data products were retrieved from the online Data Pool, courtesy of the NASA Land Processes Distributed Active Archive Center (LP DAAC), USGS/Earth Resources Observation and Science (EROS) Center, Sioux Falls, South Dakota, https://lpdaac.usgs.gov/dataset_discovery/modis/modis_products_table/mcd12q1 and .https://lpdaac.usgs.gov/data_access/data_pool.
The SRTM data products were retrieved from the online Data Pool, courtesy of the NASA Land Processes Distributed Active Archive Center (LP DAAC), USGS/Earth Resources Observation and Science (EROS) Center, Sioux Falls, South Dakota, https://lta.cr.usgs.gov/SRTMVF and https://lpdaac.usgs.gov/data_access/data_pool
Wang, L.,Qu, J., 2007. NMDI: A normalized multi-band drought index for monitoring soil and vegetation moisture with satellite remote sensing. Geophysical Research Letters 34, 1–5. doi:10.1029/2007GL031021

Weirich, F., Blesius, L., 2007. Comparison of satellite and air photo based landslide susceptibility maps. Geomorphology 87 (4), 352–364.

Xu, C., X. Xu, and J. B. H. Shyu, 2014: Field investigations of landslides triggered by the 20 April 2013 Mw 6.6 Lushan earthquake of China. *Geomorphology*, 16, 41202235, doi:10.1007/s10346-013-0404-6. http://dx.doi.org/10.1016/j.geomorph.2015.07.002.

Zhao, C., Lu, Z., Zhang, Q., & de La Fuente, J., 2012. Large-area landslide detection and monitoring with ALOS/PALSAR imagery data over Northern California and Southern Oregon, USA. Remote Sensing of Environment, 124, 348-359.

Table Captions List:

1. **Table 1:** *Temporal relationships in soil moisture for the three outcomes for this indicator*.
2. **Table 2:** *Validation results for the sampled SLIP detections. High confidence landslides are detections in which both reviewers classified an event as a landslide. Low confidence landslides are detections in which one of the two reviewers classified an event as a landslide. Tiles with majority agricultural land cover are highlighted and are found to have a lower overall accuracy.*

Figure Captions List

1. **Figure 1:** *The Nepal study area shows dramatic elevation changes from the southern area bordering India to the northern region bordering China. Landslides from the Global Landslide Catalog (Kirschbaum et al., 2015) from 2007-2016 are shown in red to demonstrate the widespread distribution of landslides in the region.*
2. **Figure 2:** *Nepal Slope Pixel Frequency derived from SRTM and ASTER DEMs, with slope classification values used for this study*
3. **Figure 3:** *The Jure Sunkoshi Landslide, occurring on August, 2nd, 2014, was used for calibration and testing in earlier iterations of the SLIP algorithm. Here it is shown prior to (left) and after (middle) the landslide. The SLIP detection with a Landsat 8 base map is shown (right) from the same Sept 18th image, with the SLIP pixel detection highlighting where the soil moisture criteria (yellow) or both red reflectance and soil moisture criteria (red) are met.*
4. **Figure 4:** *DRIP makes rainfall accumulation maps in 24, 48, and 72-hour moving windows, which can be compared with the 16-day time Landsat 8 image revisit time. The maps pinpoint regions where rainfall accumulations exceed established thresholds for rainfall triggered landslides.*
5. **Figure 5:** *Workflow showing data processing architecture of SLIP and DRIP.*
6. **Figure 6:** *The Landsat tiles used for validation of SLIP. For validation, two SLIP detections were selected for each tile to represent monsoon (June-October) and dry season conditions.*
7. **Figure 7:** *Example validation Results for each classification category: a.) Forest Landslide; b.) Glacier Melt Landslide c.) Barren d.) Agriculture e.) Riverbed f.) Urban g.) Mountainside/No Vegetation Change h.) Terrace.*
8. **Figure 8:** *Half Hourly IMERG Precipitation around Jure Sunkoshi landslide from Sept 25- August 5, 2014. The 24-hour period before the landslide is marked in blue; there is 19.5mm of rainfall in the hour just before the landslide and the second blue line is when the landslide occurred. (Data is available from giovanni.sci.gsfc.nasa.gov)*

Tables

	Today	Historic	Change
Outcome 1	1 (has moisture)	0 (no moisture)	1-0= 1 (new moisture area)
Outcome 2	1 (has moisture)	1 (has moisture)	1-1= 0 (no moisture change)
Outcome 3	0 (no moisture)	1 (has moisture)	0-1= -1 (moisture decrease)

Table 1: Temporal relationships in soil moisture for the three outcomes for this indicator

Path	Row	Julian Date	Year	Monsoon Season	Number of Validated Potential Landslide Detections (PLDs)	High Confidence Landslides (%)	Low Confidence Landslides (%)	Combined Landslide Confidence (%)	Commission Errors
140	41	254	2014	Y	83	57	26	83	36
140	41	81	2015	N	91	42	30	69	52
141	***41***	***245***	***2014***	***Y***	***22***	***13***	***19***	***31***	***19***
141	***41***	***88***	***2015***	***N***	***99***	***26***	***33***	***59***	***73***
142	40	268	2014	Y	71	36	25	61	45
142	40	79	2015	N	96	28	38	67	68
143	40	227	2014	Y	70	21	33	55	55
143	40	38	2015	N	70	18	53	71	57
144	***40***	***234***	***2014***	***Y***	***69***	***18***	***12***	***29***	***56***
144	***40***	***77***	***2015***	***N***	***54***	***14***	***18***	***32***	***46***
				AVERAGE		**27**	**29**	**56**	

Table 2: Validation results for the sampled SLIP detections. High confidence landslides are detections in which both reviewers classified an event as a landslide. Low confidence landslides are detections in which one of the two reviewers classified an event as a landslide. Tiles with majority agricultural land cover are highlighted and are found to have a lower overall accuracy.

Figures

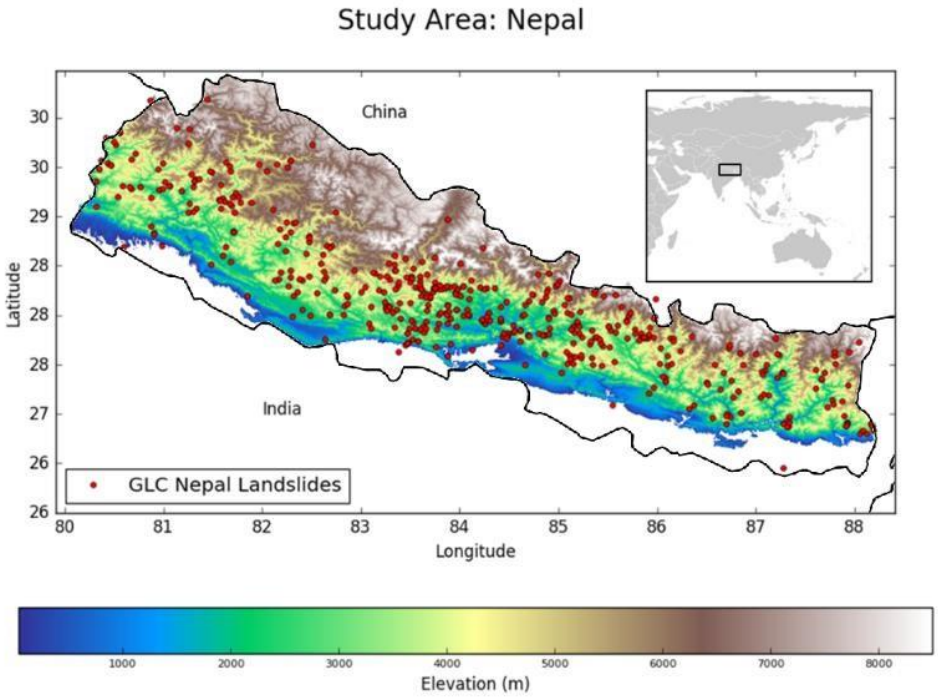

Figure 1: The Nepal study area shows dramatic elevation changes from the southern area bordering India to the northern region bordering China. Landslides from the Global Landslide Catalog (Kirschbaum et al., 2015) from 2007-2016 are shown in red to demonstrate the widespread distribution of landslides in the region.

708

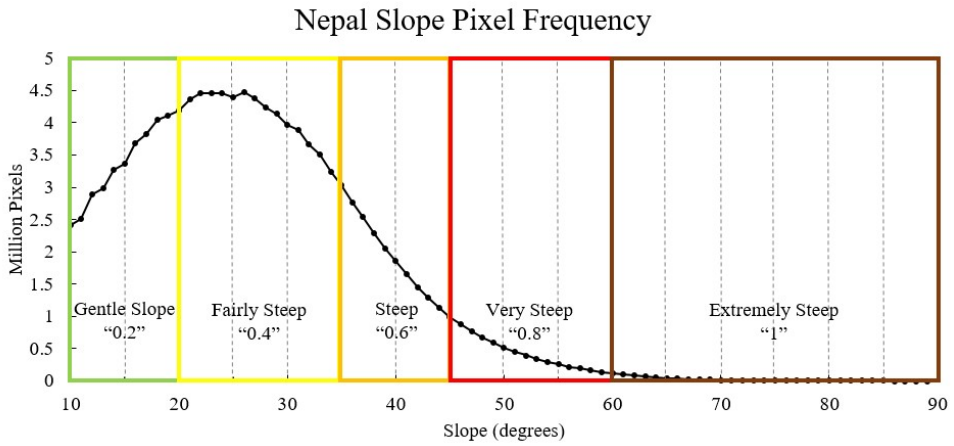

709

710 *Figure 2: Nepal Slope Pixel Frequency derived from SRTM and ASTER DEMs, with slope*
711 *classification values used for this study.*

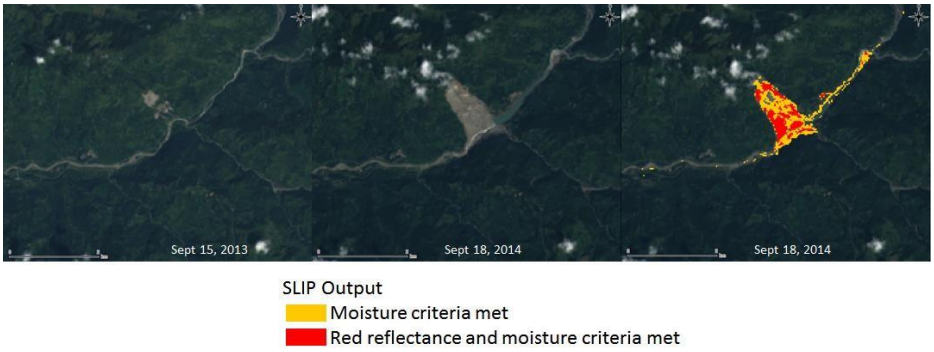

Figure 3: The Jure Sunkoshi Landslide, occurring on August, 2nd, 2014, was used for calibration and testing in earlier iterations of the SLIP algorithm. Here it is shown prior to (left) and after (middle) the landslide. The SLIP detection with a Landsat 8 base map is shown (right) from the same Sept 18th image, with the SLIP pixel detection highlighting where the soil moisture criteria (yellow) or both red reflectance and soil moisture criteria (red) are met.

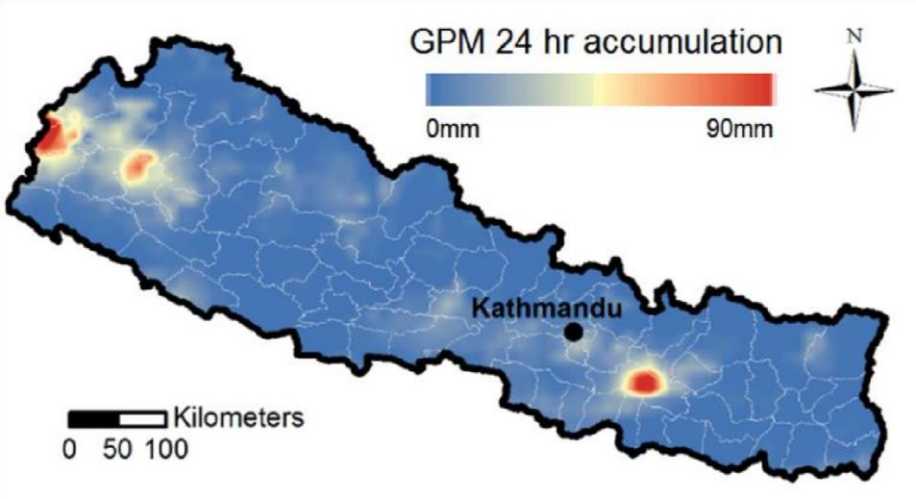

Figure 4: DRIP makes rainfall accumulation maps in 24, 48, and 72-hour moving windows, which can be compared with the 16-day time Landsat 8 image revisit time. The maps pinpoint regions where rainfall accumulations exceed established thresholds for rainfall triggered landslides.

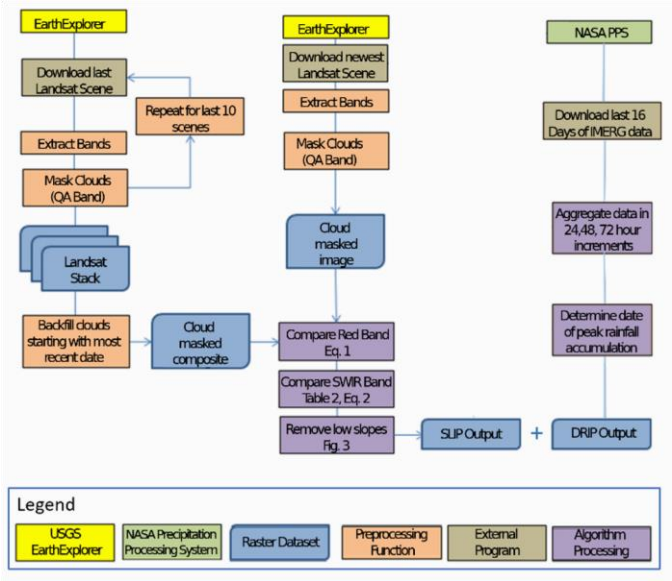

722

723 *Figure 5. Workflow showing data processing architecture of SLIP and DRIP.*

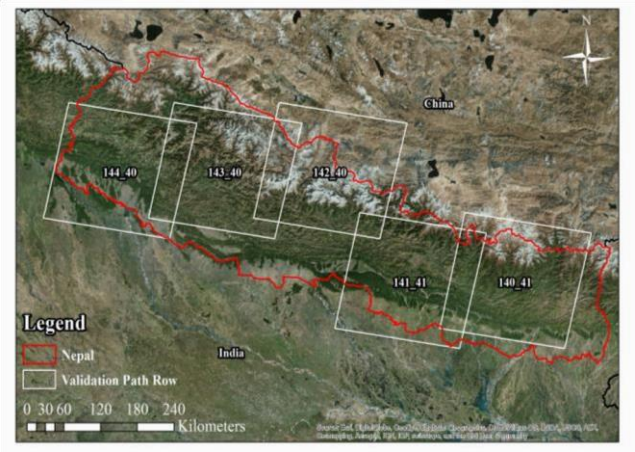

Figure 6: The Landsat tiles used for validation of SLIP. For validation, two SLIP detections were selected for each tile to represent monsoon (June-October) and dry season conditions.

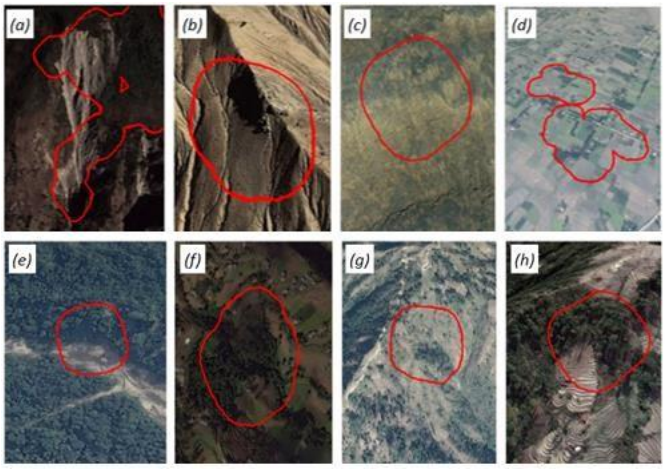

Figure 7: Example validation Results for each classification category: a.) Forest Landslide; b.) Glacier Melt Landslide c.) Barren d.) Agriculture e.) Riverbed f.) Urban g.) Mountainside/No Vegetation Change h.) Terrace.

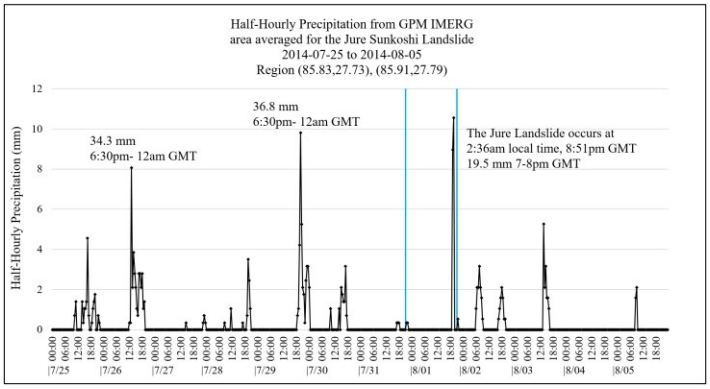

Figure 8: Half Hourly IMERG Precipitation around Jure Sunkoshi landslide from Sept 25- August 5, 2014. The 24-hour period before the landslide is marked in blue; there is 19.5mm of rainfall in the hour just before the landslide and the second blue line is when the landslide occurred. (Data is available from giovanni.sci.gsfc.nasa.gov)